Dual-Frequency Metal Object Detection Based on SPWM Control for Wireless EV Charging System

Chenyang Xia, *Member, IEEE*, Yuheng Cao, Ziyue Yang, Shuze Zhao, Xirui Wang, Chenhao Lu, and Leilei Liu

***Abstract*—Metal object detection (MOD) is an essential auxiliary function for wireless electric vehicle charging (WEVC) systems. However, current systems suffer from poor independence, low detection sensitivity, and failures at single detection frequencies. To this end, this article proposes a dual-frequency metal object detection (DF-MOD) technology based on sinusoidal pulsewidth modulation (SPWM) control for WEVC systems. The article first introduces the system structure and working principle, then establishes an equivalent model of the DF-MOD and analyzes its operational characteristics. Subsequently, the parameters for the main circuit and the filter circuit are designed to further enhance the detection sensitivity and anti-interference capability of the DF-MOD system. Finally, a system experimental platform is constructed to verify the feasibility and superiority of the DF-MOD technology controlled by SPWM in WEVC systems. The results indicate that the system achieves independent operation from the WEVC systems and improves detection sensitivity for 40×40 mm copper plates, aluminum plates, iron plates, and ferrite plates by 7.56%, 5.59%, 5.36%, and 16.82%, respectively, compared to single-frequency detection. Additionally, it achieves blind spot-free detection across the entire area.**

***Index Terms*—Dual-frequency, metal object detection (MOD), sinusoidal pulsewidth modulation (SPWM) control, wireless electric vehicle charging (WEVC).**

I. Introduction

With widespread attention and promotion worldwide in recent years, electric vehicle (EV) has become increasingly prominent [1], [2]. Currently, traditional plug-in charging modes for EVs suffer from inconveniences such as plug aging [3]. It is recognized that applying wireless power transfer technology to EV charging provides advantages over traditional plug-in charging [4], [5], [6].

The wireless electric vehicle charging (WEVC) system efficiently transmit energy through high-frequency magnetic fields. However, metal object (MO) in the magnetic coupling area can induce eddy effect and magnetization effect [7]. Not only does this impact the efficiency and output power of the system, but it also raises the temperature of MOs due to eddy current effect [8]. Consequently, this can lead to fires, resulting in potential losses to people's lives and property safety. Therefore, metal object detection (MOD) technology has become one of the indispensable auxiliary functions of WEVC systems [9].

Nowadays, the MOD technology mainly relies on methods based on nonelectrical parameter sensors [10], methods based on parameters of the WEVC [11], [12], and methods based on detection coils [13], [14]. Analysis indicates that the coil-based MOD method provides advantages such as simplicity in principle, high expandability of auxiliary functions, and lower costs. making it the mainstream research direction. With its numerous advantages, the coil-based MOD method has not only emerged as the dominant research focus but also prompted further specialization, leading to the distinction between active and passive detection coil methodologies.

1) In the first category, the detection coil is powered by an external power source. By measuring the impedance change of the coil, the detection function is achieved due to the intervention of MOs in the magnetic field. Jeong et al. [15] designed a parallel resonant amplification circuit, where the entry of MOs into the detection magnetic field causes circuit detuning, resulting in voltage variations and enabling the detection of MOs. Li et al. [16] and Xia et al. [17] proposed a detection coil mode based on changes in phase difference, facilitating the detection of small MOs by monitoring phase differences. Sun et al. [18] introduced a detection method based on changes in quality factor of the detection coil at multiple frequencies. Although the active coil-based MOD method provides advantages such as independent operation and absence of blind spots, its circuitry is complex and costs are higher.
2) In the second category, induced voltage is generated in the detection coil by exciting the magnetic field, without the need for a separate power supply. When MOs enter the detection magnetic field, they affect the impedance parameters of the detection coil and the coupling coefficient between the detection coil and the excitation magnetic field. This leads to variations in induced voltage, enabling detection. According to the method of generating the excitation magnetic field, it can be categorized into passive excitation and active excitation methods.

Received 11 June 2024; revised 17 August 2024; accepted 2 October 2024. Date of publication 7 October 2024; date of current version 12 December 2024. This work was supported in part by the National Natural Science Foundation of China under Grant 52277020 and in part by the Natural Science Foundation of Jiangsu Province under Grant BK20211246. Recommended for publication by Associate Editor C. Lee. *(Corresponding author: Chenyang Xia.)*

The authors are with the School of Electrical Engineering, China University of Mining and Technology, Xuzhou 221116, China (e-mail: chyxia@cumt.edu.cn; caoyh666@cumt.edu.cn; yang.ziyue@cumt.edu.cn; zhaoshuze@cumt.edu.cn; wangxirui@cumt.edu.cn; ts22230127p31@cumt.edu.cn; ts22230040a31@cumt.edu.cn).

Color versions of one or more figures in this article are available at https://doi.org/10.1109/TPEL.2024.3474691.

Digital Object Identifier 10.1109/TPEL.2024.3474691

a) Passive excitation method utilizes the power magnetic field used in WEVC to detect. For instance, Xiang et al. [19] proposed a dual-layer symmetrical detection coil configuration for detecting the presence and location of foreign objects. Niu et al. [20] designed a nonaxisymmetric detection coil configuration to eliminate central blind spots. The passive excitation method features a simple structure and lower cost. However, it must rely on the power magnetic field generated by the transmitting coil, which cannot operate independently and is easily affected by power fluctuations.

b) Active excitation method involves generating a detection magnetic field with a frequency significantly different from that of the power magnetic field to avoid interference. For instance, Qi et al. [21] utilized a dual resonant circuit to isolate the seventh harmonic components of energy transmission for MOD. By enhancing the eddy current effect through high-frequency detection, it improves detection sensitivity to some extent. However, this method, which relies on the harmonics of the power system, still cannot achieve independent operation of the metallic foreign object detection system. Zhao et al. [22] proposed an external bipolar checkerboard excitation coil to generate an excitation magnetic field for metallic foreign object detection, eliminating the magnetic field blind spots caused by the transmitting coil's structure while decoupling from the power magnetic field. However, this method has a single detection frequency and cannot avoid detection failure caused by the cancellation of eddy effect and magnetization effect.

Through the above mentioned analysis, it can be seen that MOs generate eddy effect and magnetization effect in the magnetic field, causing changes in detection coil parameters and the coupling coefficient of the detection magnetic field. MOD is achieved by directly or indirectly monitoring these parameter changes. However, due to the combined influence of eddy effect and magnetization effect, detection effectiveness varies for the same metal at different frequencies and interacts with several different metals, and a single frequency may even lead to detection failure for certain metals. Therefore, a flexible dual-frequency MOD technology is needed to meet the requirements of independent operation and blind-spot-free detection in EV applications. This approach will further enhance the sensitivity and accuracy of MOD.

Sinusoidal pulsewidth modulation (SPWM) control is a method that uses the comparison of a carrier wave and a modulation wave to control an inverter and achieve the desired waveform output [23], [24], [25]. It offers advantages such as easy adjustment of output frequency and voltage. This article proposes a dual-frequency MOD (DF-MOD) method for WEVC system using the high-frequency harmonic characteristics of SPWM modulation.

The rest of this article is organized as follows. Section II introduces the system structure and working principle. Section III discusses the establishment of an equivalent model of the DF-MOD system and analyzes the working characteristics of the DF-MOD system. In Section IV, parameter design for main circuit and signal processing circuit was conducted through simulation analysis, thereby further enhancing the sensitivity and anti-interference capability of MOD. Experimental process and results are provided in Section V, where a system test platform is constructed to verify the feasibility and superiority of SPWM-controlled DF-MOD in WEVC systems. Finally, Section VI concludes this article.

II. Structure and Working Principle of the System

A. Structure of Proposed System

1) Introduction of System Circuit Structure: The proposed SPWM-controlled DF-MOD in WEVC systems is shown in Fig. 1.

The system mainly consists of two parts: WEVC and the DF-MOD. The WEVC system operates at a frequency of $f_t = 85$ kHz. The DF-MOD system utilizes a dual-frequency composite magnetic field generated by the SPWM-controlled inverter's output voltage fundamental component ($f_s = 8.5$ kHz) and carrier frequency component ($f_h = 850$ kHz) for detection. Both systems can operate independently without interference.

The ground side of the WEVC consists of a dc power supply V, a high-power inverter, a transmitting coil, and its compensation circuit. The EV receiving side comprises a receiving coil, its compensation circuit, and a load circuit.

The DF-MOD system consists of three parts as follows.

a) Excitation circuit of DF-MOD: This circuit includes a dc power supply V_{in}, a full-bridge inverter circuit, an SPWM control circuit, a DF-Resonant Circuit, and a set of excitation coils. The SPWM modulation carrier wave u_c is an 850 kHz triangular wave, and the modulation wave u_h is an 8.5 kHz sine wave. The digital signal processing (DSP) controls the SPWM to generate switching signals, enabling the full-bridge inverter circuit to convert the dc voltage V_{in} into an ac voltage U_e. The DF-resonant circuit selects the fundamental frequency voltage component U_{es} and the carrier frequency voltage component U_{eh}, generating a dual-frequency detection magnetic field through the excitation coil.

b) Detection circuit of DF-MOD: This circuit includes of a set of detection coils, a low-frequency sampling circuit (LF-sampling circuit), and a high-frequency sampling circuit (HF-sampling circuit). The detection coil receives the DF-detection magnetic field. An 850 kHz wave trapper, composed of L_h and C_h, along with the low-frequency resonant compensation capacitor C_{ds} and the low-frequency sampling resistor R_{ds}, captures the low-frequency detection signal. An 8.5 kHz wave trapper, composed of L_s and C_s, along with the high-frequency resonant compensation capacitor C_{dh} and the high-frequency sampling resistor R_{dh}, captures the high-frequency detection signal. The specific circuit structure is shown in Fig. 6.

c) Signal processing circuit of DF-MOD: This circuit includes the low-frequency signal processing circuit (LF-signal processing circuit) and the high-frequency signal processing circuit (HF-signal processing circuit). The low-frequency detection circuit receives the low-frequency voltage U_{ds} across the low-frequency sampling resistor R_{ds}. The low-frequency signal passes through a low-pass filter (LPF) circuit, a noninverting

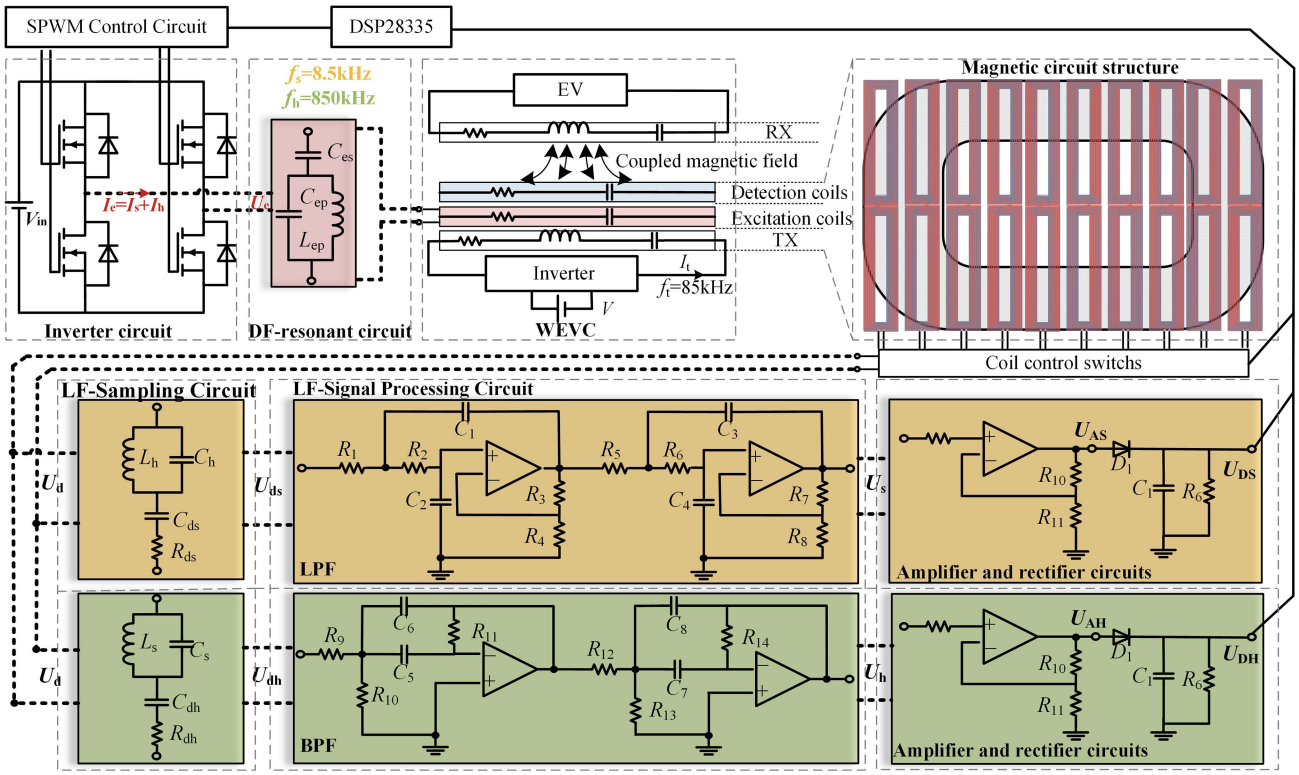

Fig. 1. Structure diagram of the SPWM-controlled DF-MOD system.

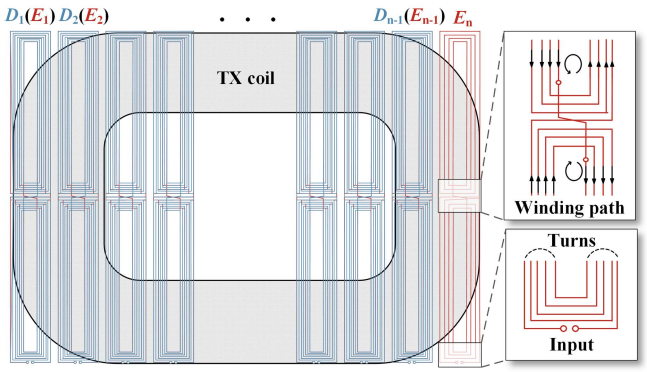

Fig. 2. Magnetic circuit structure of DF-MOD.

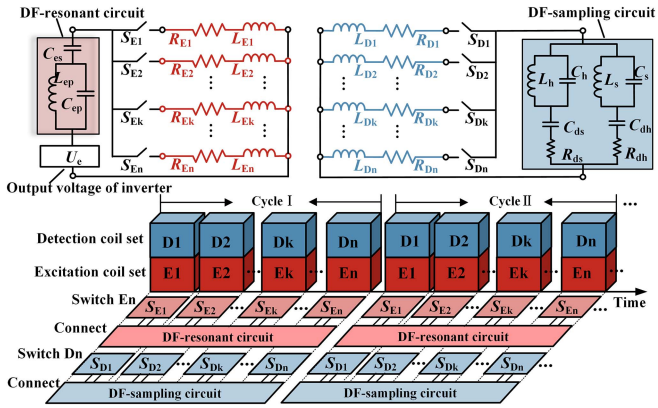

Fig. 3. Working mode of DF-MOD.

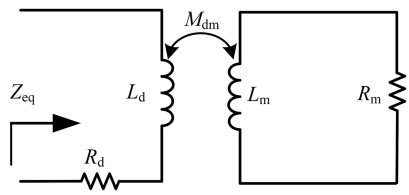

Fig. 4. Equivalent circuit model of detection coil of MOs intrusion.

amplifier, and a rectifier circuit to output a dc voltage signal U_{DS}. The high-frequency detection circuit receives the high-frequency voltage U_{dh} across the high-frequency sampling resistor R_{dh}. The high-frequency signal passes through a band-pass filter (BPF) circuit, a noninverting amplifier, and a rectifier circuit to output a dc voltage signal U_{DH}. The dc voltage signals U_{DS} and U_{DH} are compared with threshold voltages to determine the presence of metallic foreign objects.

2) Magnetic Circuit Structure and Operation of the System: The magnetic circuit structure of the DF-MOD system is shown in Fig. 2. The set of excitation coils is placed directly above the transmitting coil, with the set of detection coils covering it and having the same dimensions. Based on the study in [22], both the set excitation coils (E_1-E_n) and the set of detection coils (D_1-D_n) adopt a bipolar structure formed by two subcoils connected in series with opposite directions. Compared to the differential detection method using symmetric coils, this design

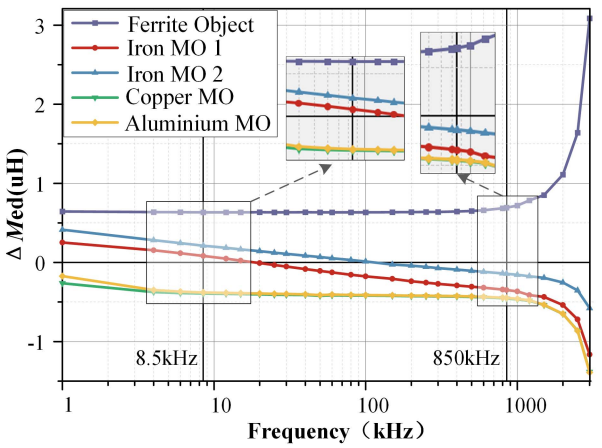

Fig. 5. Relationship between the frequency and ΔM_{ed}.

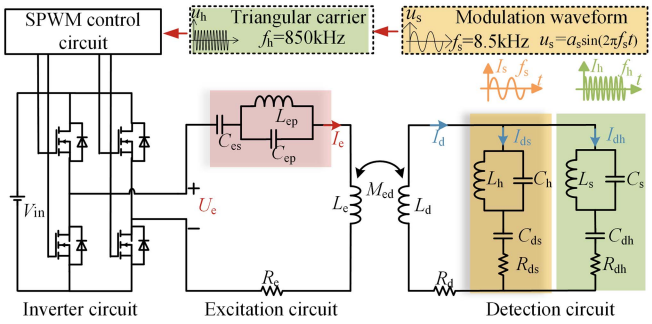

Fig. 6. Simplified equivalent circuit model of DF-MOD.

eliminates the detection blind spot at the symmetric center, effectively suppresses noise from the power magnetic field.

To simplify the system structure and reduce production costs, the DF-MOD system uses a time-division multiplexing (TDM) method. This working mode, as shown in Fig. 3, enables full-area detection of MOs.

In Fig. 3, the excitation coils are represented as an inductance $L_{\mathrm{E}n}$ in series with a resistance $R_{\mathrm{E}n}$. The excitation switches $S_{\mathrm{E}1}$-$S_{\mathrm{E}n}$ control the connection of the excitation coil set E_1-E_n to the excitation circuit. Similarly, the detection coils are represented as an inductance $L_{\mathrm{D}n}$ in series with a resistance $R_{\mathrm{D}n}$. The detection switches $S_{\mathrm{D}1}$-$S_{\mathrm{D}n}$ control the connection of the detection coil set D_1-D_n to the DF-detection circuit. In this article, there are 13 groups of excitation and detection coils, and the working time of a single detection coil is designed to be 50 ms. The total time duration of one cycle of system operation is 0.65 s. The sets of coils operate in a cyclical sequence until a MO is detected, at which point the system stops and reports the identification number of the detection coil where the object is found.

B. Working Principle

1) Principle of MOD: When a metal object enters the magnetic field, it generates eddy current and magnetization effects. These effects alter the spatial magnetic field intensity and the impedance parameters of the detection coil. The eddy effect induced by the MOs can be modeled as a series combination of inductance and resistance. The equivalent circuit of the detection coil with the MOs is shown in Fig. 4.

In Fig. 4, R_{m} and L_{m} represent the equivalent resistance and inductance of the MO, while R_{d} and L_{d} represent the resistance and inductance of the detection coil. M_{dm} represents the mutual inductance between the detection coil and the MO. Considering the combined effects of eddy current and magnetization effects, the equivalent resistance and inductance of the detection coil change. After the entry of a MO, they are expressed as

$$R_{\mathrm{eq-m}} = R_{\mathrm{d}} + \frac{R_{\mathrm{m}}(\omega M_{\mathrm{dm}})^2}{R_{\mathrm{m}}^2 + (\omega L_{\mathrm{m}})^2} \tag{1}$$

$$L_{\mathrm{eq-m}} = L_{\mathrm{d}} - \frac{L_{\mathrm{m}}(\omega M_{\mathrm{dm}})^2}{R_{\mathrm{m}}^2 + (\omega L_{\mathrm{m}})^2} + L_{\mathrm{M}} \tag{2}$$

where L_{M} represents the part of the equivalent inductance increase caused by the magnetization effect of ferromagnetic metals. Nonferromagnetic metals (such as copper, aluminum, gold, and silver) primarily produce eddy current effect in high-frequency magnetic fields, with negligible magnetization effect. Ferromagnetic metals (such as iron, nickel, and cobalt) generate both eddy current and magnetization effects in high-frequency magnetic fields. According to electromagnetic field theory, the magnetization effect of ferromagnetic MOs depends solely on the relative permeability of the magnetic field and is not influenced by the magnetic field frequency. In contrast, the eddy current effect becomes more pronounced with increasing magnetic field frequency.

Due to the eddy current effect weakening the detection magnetic field and the magnetization effect enhancing it, the impact of increasing magnetic field frequency on the detection of ferromagnetic MOs is uncertain. Fig. 5 shows the variation in mutual inductance between the detection coil and the excitation coil for common foreign objects (FOs) under detection magnetic fields of different frequencies.

Fig. 5 shows that nonferromagnetic MOs do not exhibit magnetization effects. As frequency increases, their eddy effects become more significant. For ferromagnetic MOs, at low frequencies, the magnetization effect is greater than the eddy current effect, resulting in an increase in mutual inductance. As the frequency increases, the eddy effect becomes dominant, leading to a decrease in mutual inductance. Ferrite materials, which only exhibit magnetization effects without generating eddy currents, show an increase in mutual inductance. Therefore, for ferromagnetic metals, using a single frequency detection magnetic field may cause the eddy current effect and magnetization effect to cancel each other out, resulting in detection failure. Selecting high and low frequency detection with a large difference can avoid this phenomenon.

In this article, the electric vehicle wireless charging system adopts the inverter circuit of H-bridge structure, and its operating frequency is 85 kHz, so there will be 85 kHz odd multiple frequency harmonics in the output current. The 85 kHz fundamental frequency and 85 kHz odd times harmonic frequency of the electric vehicle wireless charging system will have an

impact on the detection effect of the proposed MOD system, so it is necessary to reduce this part of the impact by selecting the operating frequency of the MOD system, and the specific selection basis is as follows.

1) The interference of 85 kHz fundamental frequency to the proposed MOD system is mainly eliminated by active filter circuit, in order to achieve better detection effect, the detection frequency and the interference frequency should be 10 times or more;
2) In order to reduce the interference of the 85 kHz odd times frequency harmonics, the high frequency detection frequency of the metal foreign object detection should be set as the even times frequency of 85 kHz.
3) Since the inverter circuit of the H-bridge structure needs to set the dead time to avoid the bridge arm straight-through, it will affect the harmonic spectrum of the output current at high operating frequency, which will be detrimental to the design of the active filter circuit.
4) Additionally, due to the skin effect, the internal resistance of the coil increases sharply at high frequencies, complicating system parameter design. Conversely, if the detection frequency is too low, the induced voltage in the detection coil becomes too small, making it difficult to observe changes in the detection voltage.

Taking the above factors into consideration, we set the detection frequencies of the MOD system to 850 kHz and 8.5 kHz.

2) Principle of SPWM-Controlled DF-Magnetic Field Transmission and Reception: The SPWM-controlled method proposed in this article achieves the generation of the low-frequency magnetic field by modulating the frequency component of the inverter output voltage. The high-frequency magnetic field is generated through the carrier frequency component of the output voltage.

The advantages of the SPWM method over TDM are as follows: it is able to output 8.5 kHz and 850 kHz signals simultaneously, eliminating the need to set up separate excitation power supplies for 8.5 kHz and 850 kHz; a single power supply is used, eliminating the need for hardware switching of power supply circuits; it is able to speed up the detection time of foreign objects, improving the safety of the wireless charging system for electric vehicles. Fig. 6 illustrates the schematic diagram of the system principle.

The commonly used modulation methods for SPWM can be divided into three types: 1) unipolar modulation, 2) unipolar frequency doubling modulation, and 3) bipolar modulation. Among them, bipolar modulation method is more flexible and has higher controllability. According to the Fourier decomposition formula, the expressions for the fundamental component and harmonic components of the output voltage can be obtained when using bipolar SPWM modulation, as shown

$$u_{\mathrm{e}} = a_{\mathrm{s}} V_{\mathrm{in}} \sin \omega_{\mathrm{s}} t + \frac{4V_{\mathrm{in}}}{m\pi} J_i\left(\frac{a_{\mathrm{s}} m\pi}{2}\right) \sin\left[(m\omega_{\mathrm{h}} \pm i\omega_{\mathrm{s}})\, t + \theta\right] \tag{3}$$

where V_{in} represents the magnitude of the dc voltage source, a_{s} denotes the modulation index, ω_{s} stands for the modulation wave angular frequency, and ω_{h} is the carrier wave angular frequency. J_i denotes the ith order Bessel function, where i is even when m is odd, and i is odd when m is even. As indicated by the formula, the harmonic component in the output voltage is highest at the carrier frequency. Therefore, this study selects the voltage components of the fundamental frequency and the carrier frequency in the output voltage to realize the DF-magnetic field for MOD. Fig. 7 illustrates the magnitudes of the fundamental and carrier components of the output voltage under different modulation indices.

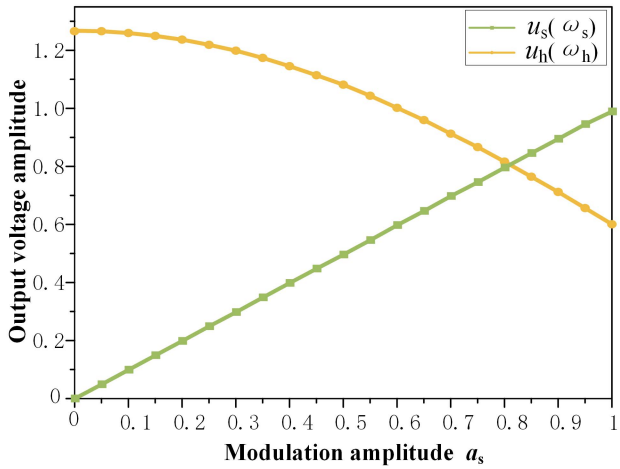

Fig. 7. Relationship between the a_{s} and output voltage.

From Fig. 7, it can be observed that the fundamental voltage amplitude of the SPWM-controlled inverter output increases linearly with the modulation index, while the harmonic amplitude at the carrier frequency decreases more rapidly as the modulation index increases. Therefore, setting the modulation index appropriately can yield a dual-frequency power source suitable for this system.

a) DF-resonant circuit parameter design guidelines: The excitation coil significantly impedes the flow of high-frequency current alone. To generate a DF-magnetic field while minimizing the impact of other frequency harmonics and power magnetic fields, a DF-resonance circuit, consisting of C_{es}, C_{ep}, and L_{ep}, is constructed. Its equivalent impedance expression Z_{e} is obtained by

$$\begin{aligned} Z_{\mathrm{e}} &= j\omega L_{\mathrm{e}} + \frac{1}{j\omega C_{\mathrm{es}}} + \frac{1}{\frac{1}{j\omega L_{\mathrm{ep}}} + j\omega C_{\mathrm{ep}}} + R_{\mathrm{e}} \\ &= R_{\mathrm{e}} + \frac{L_{\mathrm{ep}} C_{\mathrm{ep}} L_{\mathrm{e}} C_{\mathrm{es}} \omega^4 - (L_{\mathrm{ep}} C_{\mathrm{ep}} + L_{\mathrm{e}} C_{\mathrm{es}} + L_{\mathrm{ep}} C_{\mathrm{es}})\omega^2 + 1}{j\omega C_{\mathrm{ep}} (1 - \omega^2 L_{\mathrm{ep}} C_{\mathrm{ep}})}. \end{aligned} \tag{4}$$

From (4), it can be seen that this topology has two functions. It traps a specific frequency by making the denominator of the imaginary part of the equivalent impedance of the excitation circuit zero. Additionally, it achieves series resonance at two frequencies by making the numerator of the imaginary part of the equivalent impedance zero.

To achieve series resonance at frequencies f_s and f_h, the parameters must satisfy the following constraints [20]:

$$\begin{cases} \omega_t = 2\pi f_t, \omega_s = 2\pi f_s, \omega_h = 2\pi f_h \\ \frac{1}{\sqrt{L_{ep}C_{ep}}} = \omega_t \\ \frac{1}{\sqrt{L_e C_{es}}} = \frac{\omega_s \omega_h}{\omega_t} \\ \frac{1}{\sqrt{L_{ep}C_{es}}} = \frac{\omega_t \omega_s \omega_h}{\sqrt{\omega_t{}^2\omega_s{}^2+\omega_t{}^2\omega_h{}^2-\omega_s{}^2\omega_h{}^2-\omega_t{}^4}} \end{cases} \tag{5}$$

where f_t is designed to be 85 kHz, causing C_{ep} and L_{ep} to form a parallel resonance, thereby preventing the excitation coil from generating induced currents due to the power magnetic field. The modulation wave frequency f_s is 8.5 kHz, and the carrier frequency f_h is 850 kHz. By calculation, the parameters of the dual-frequency network that satisfy series resonance at frequencies of 8.5 kHz and 850 kHz, and trap the 85 kHz signal, can be determined.

b) LF-sampling circuit parameter design guidelines: Referring to (4), to achieve simultaneous detection of DF-signals, the LF-sampling circuit is composed of L_h and C_h in parallel resonance, forming a wave trappeer with a frequency of 850 kHz. This wave trapper is inductive at the low frequency of 8.5 kHz. Therefore, in the LF-sampling circuit, serial compensation capacitance C_{ds} is introduced to form a serial resonance at a frequency of 8.5 kHz with the detection coil. At this point, the voltage across the LF-sampling resistor R_{ds} corresponds to the LF-sampling voltage at 8.5 kHz. Consequently, the following constraints must be taken into account:

$$\begin{cases} \frac{1}{\omega_h C_h} = \omega_h L_h \\ \frac{1}{\omega_s C_{ds}} = \omega_s L_d + \frac{\omega_s L_h}{1-\omega_s{}^2 L_h C_h}. \end{cases} \tag{6}$$

c) HF-sampling circuit parameter design guidelines: In the high-frequency sampling circuit, L_s and C_s form a wave trapper for 8.5 kHz. The parallel resonance network is capacitive at the high frequency of 850 kHz. However, it does not fully compensate for the HF-detection circuit. Therefore, a series compensation capacitor C_{dh} is required. This forms a series resonance at 850 kHz with the detection coil and the HF-sampling circuit. Consequently, the following constraints must be taken into account:

$$\begin{cases} \frac{1}{\omega_s C_s} = \omega_s L_s \\ \frac{1}{\omega_h C_{dh}} = \omega_h L_d - \frac{\omega_h L_s}{1-\omega_h{}^2 L_s C_s}. \end{cases} \tag{7}$$

The output voltage of the detection coil is processed through both the LF- and HF-sampling circuits to extract the corresponding frequency signals. These signals then pass through subsequent signal processing circuits, which consist of active filter circuits, amplification circuits, and rectification circuits, enabling dual-frequency detection of MOs.

III. Equivalent Model Establishment and Characteristic Analysis of the Proposed System

A. Establishment of the Equivalent Model for the DF-MOD System

The magnetic field generated by the transmitting coil is unipolar. The induced currents $I_{t\text{-}d}$ in the two opposing subcoils of the detection coil are in opposite directions and equal in magnitude, thus canceling each other out and avoiding power loss caused by the power magnetic field and overvoltage damage to the detection circuit [13], [17], [22]. However, the excitation coil current I_e creates magnetic fields in opposite directions in the regions of the two subcoils. The induced currents $I_{e\text{-}d}$ is in the same direction in both subcoils of the detection coil, which leads to the output of an induced voltage. Fig. 8 illustrates the decoupling of the DF-MOD system.

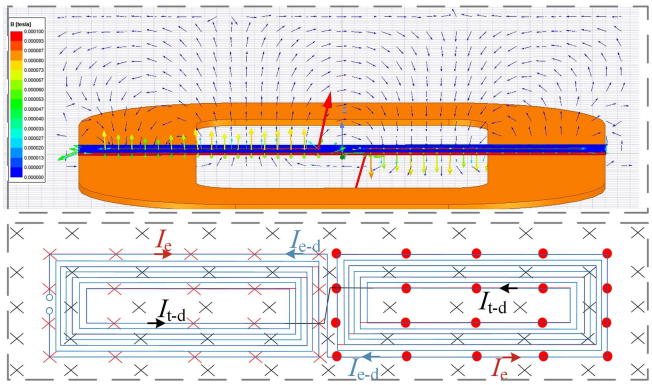

Fig. 8. Schematic diagram of decoupling the detection magnetic field from the power magnetic field.

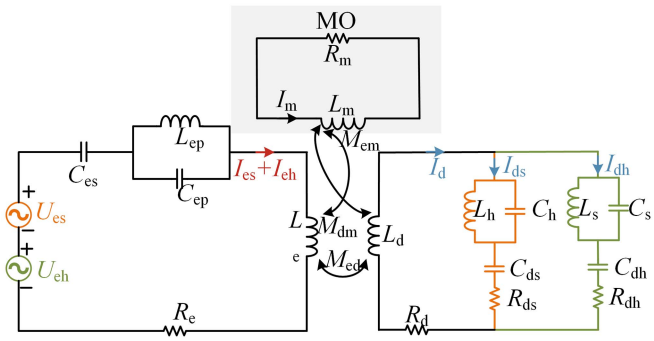

Fig. 9. Equivalent circuit model of DF-MOD with MO intrusion.

The decoupling of the detection magnetic field from the power magnetic field is achieved. The equivalent circuit model of the detection system with MO intrusion is established, as shown in Fig. 9.

According to the superposition theorem of circuits, the fundamental component of the output voltage U_e of the SPWM-controlled inverter and the harmonic components of the carrier magnitude can be equivalently represented as a LF-voltage source U_{es} and a HF-voltage source U_{eh}.

1) Establishment of the Equivalent Model for LF-MOD: At the low frequency of $f_s = 8.5$ kHz, the components L_s and C_s in the HF-sampling circuit undergo parallel resonance, making the HF-sampling circuit equivalent to an open circuit. Similarly, at the high frequency $f_h = 850$ kHz, the components L_h and C_h in the low-frequency sampling circuit undergo parallel resonance. So, there is no high-frequency signal interference in the LF-sampling circuit. When no MO is present in the detection area,

the system is equivalent to a two-coil model consisting of the excitation circuit and the LF-detection circuit. The state equation for the LF-MOD system is obtained by

$$\begin{bmatrix} U_{\mathrm{es}} \\ 0 \end{bmatrix} = \begin{bmatrix} Z_{\mathrm{es}} & -j\omega_{\mathrm{s}} M_{\mathrm{ed-s}} \\ -j\omega_{\mathrm{s}} M_{\mathrm{ed-s}} & Z_{\mathrm{ds}} \end{bmatrix} \begin{bmatrix} I_{\mathrm{es}} \\ I_{\mathrm{ds}} \end{bmatrix}. \tag{8}$$

At the low frequency of 8.5 kHz, $M_{\mathrm{ed\text{-}s}}$ represents the mutual inductance between the excitation coil and the detection coil. I_{es} and I_{ds} are the currents flowing through the excitation circuit and the LF-sampling circuit, respectively. Z_{es} and Z_{ds} are the equivalent impedances of the excitation circuit and the detection circuit when they are in resonance, with $Z_{\mathrm{es}} = R_{\mathrm{e}}$ and $Z_{\mathrm{ds}} = R_{\mathrm{d}} + R_{\mathrm{ds}}$. According to (8), the voltage expression across the LF-sampling resistor is derived as

$$U_{\mathrm{ds}} = \frac{j\omega_{\mathrm{s}} M_{\mathrm{ed-s}} U_{\mathrm{es}} R_{\mathrm{ds}}}{Z_{\mathrm{es}} Z_{\mathrm{ds}} + {\omega_{\mathrm{s}}}^2 {M_{\mathrm{ed-s}}}^2}. \tag{9}$$

When a MO enters the detection area, it can be modeled as an inductance L_{m} and resistance R_{m} in series, forming a three-coil equivalent model with the detection coil and the excitation coil. The system state equation can be expressed as

$$\begin{bmatrix} U_{\mathrm{es}} \\ 0 \\ 0 \end{bmatrix} = \begin{bmatrix} Z_{\mathrm{es}} & -j\omega_{\mathrm{s}} M_{\mathrm{ed-s}} & -j\omega_{\mathrm{s}} M_{\mathrm{em-s}} \\ -j\omega_{\mathrm{s}} M_{\mathrm{ed-s}} & Z_{\mathrm{ds}} & j\omega_{\mathrm{s}} M_{\mathrm{dm-s}} \\ j\omega_{\mathrm{s}} M_{\mathrm{em-s}} & -j\omega_{\mathrm{s}} M_{\mathrm{dm-s}} & Z_{\mathrm{ms}} \end{bmatrix} \begin{bmatrix} {I_{\mathrm{es}}}' \\ {I_{\mathrm{ds}}}' \\ {I_{\mathrm{ms}}}' \end{bmatrix} \tag{10}$$

where ${I_{\mathrm{es}}}'$, ${I_{\mathrm{ds}}}'$, and ${I_{\mathrm{ms}}}'$ are the currents induced in the excitation circuit, LF-sampling circuit, and eddy currents generated by the MO, respectively. Z_{ms} is the equivalent impedance of the MO. $M_{\mathrm{em\text{-}s}}$ is the mutual inductance between the excitation coil and the MO. $M_{\mathrm{dm\text{-}s}}$ is the mutual inductance between the detection coil and the MO. By solving the state equations, the expression for the LF-sampling voltage after the introduction of a MO can be obtained

$$U_{\mathrm{ds-m}} = \frac{j\omega_{\mathrm{s}} {M_{\mathrm{ed-s}}}' U_{\mathrm{es}} R_{\mathrm{ds}}}{{Z_{\mathrm{es}}}' {Z_{\mathrm{ds}}}' + {\omega_{\mathrm{s}}}^2 {M_{\mathrm{ed-s}}}'^2}. \tag{11}$$

Using the impedance change formulas for the detection coil derived (1) and (2), the equivalent impedance of the excitation circuit ${Z_{\mathrm{es}}}'$, the equivalent impedance of the detection circuit ${Z_{\mathrm{ds}}}'$, and the mutual inductance between the excitation coil and the detection coil ${M_{\mathrm{ed\text{-}s}}}'$ at the low frequency of 8.5 kHz can be expressed as follows:

$${Z_{\mathrm{es}}}' = R_{\mathrm{e}} + \frac{R_{\mathrm{m}}(\omega_{\mathrm{s}} M_{\mathrm{em-s}})^2}{R_{\mathrm{m}}^2 + (\omega_{\mathrm{s}} L_{\mathrm{m}})^2} - j\frac{L_{\mathrm{m}}(\omega_{\mathrm{s}} M_{\mathrm{em-s}})^2}{R_{\mathrm{m}}^2 + (\omega_{\mathrm{s}} L_{\mathrm{m}})^2} + j\omega_{\mathrm{s}} L_{\mathrm{eM}} \tag{12}$$

$${Z_{\mathrm{ds}}}' = R_{\mathrm{d}} + R_{\mathrm{ds}} + \frac{R_{\mathrm{m}}(\omega_{\mathrm{s}} M_{\mathrm{dm-s}})^2}{R_{\mathrm{m}}^2 + (\omega_{\mathrm{s}} L_{\mathrm{m}})^2} - j\frac{L_{\mathrm{m}}(\omega_{\mathrm{s}} M_{\mathrm{dm-s}})^2}{R_{\mathrm{m}}^2 + (\omega_{\mathrm{s}} L_{\mathrm{m}})^2} + j\omega_{\mathrm{s}} L_{\mathrm{dM}} \tag{13}$$

$${M_{\mathrm{ed-s}}}' = M_{\mathrm{ed-s}} - \frac{j\omega_{\mathrm{s}} M_{\mathrm{em-s}} M_{\mathrm{dm-s}}}{R_{\mathrm{m}} + j\omega_{\mathrm{s}} L_{\mathrm{m}}} + \Delta M_{\mathrm{ed}} \tag{14}$$

where L_{eM} and L_{dM} are the inductances affected by the magnetization effect of the ferromagnetic metal on the excitation coil and the detection coil. ΔM_{ed} represents the change in mutual inductance between the excitation coil and the detection coil due to the magnetization effect of the ferromagnetic metal. The voltage change caused by the entery of a metallic foreign object, derived from the sampling voltage expression, can be expressed as

$$\Delta U_{\mathrm{ds}} = \left| \frac{j\omega_{\mathrm{e}} {M_{\mathrm{ed-s}}}' U_{\mathrm{es}} R_{\mathrm{ds}}}{{Z_{\mathrm{es}}}' {Z_{\mathrm{ds}}}' + {\omega_{\mathrm{s}}}^2 {M_{\mathrm{ed-s}}}'^2} \right| - \left| \frac{j\omega_{\mathrm{s}} M_{\mathrm{ed-s}} U_{\mathrm{es}} R_{\mathrm{ds}}}{Z_{\mathrm{es}} Z_{\mathrm{ds}} + {\omega_{\mathrm{s}}}^2 {M_{\mathrm{ed-s}}}^2} \right|. \tag{15}$$

2) Establishment of the Equivalent Model for HF-MOD: Due to the HF-detection circuit being free from interference by the LF-detection signal. According to the state equations from (11) and (13) to establish and solve the state equation for high-frequency MOD. The change in HF-detection voltage ΔU_{dh} upon entry of a MO can be obtained

$$\Delta U_{\mathrm{dh}} = \left| \frac{j\omega_{\mathrm{h}} {M_{\mathrm{ed-h}}}' U_{\mathrm{eh}} R_{\mathrm{dh}}}{{Z_{\mathrm{eh}}}' {Z_{\mathrm{dh}}}' + {\omega_{\mathrm{h}}}^2 {M_{\mathrm{ed-h}}}'^2} \right| - \left| \frac{j\omega_{\mathrm{h}} M_{\mathrm{ed-h}} U_{\mathrm{eh}} R_{\mathrm{dh}}}{Z_{\mathrm{eh}} Z_{\mathrm{dh}} + {\omega_{\mathrm{h}}}^2 {M_{\mathrm{ed-h}}}^2} \right| \tag{16}$$

where R_{dh} is the high-frequency sampling resistor. $M_{\mathrm{ed\text{-}h}}$ and ${M_{\mathrm{ed\text{-}h}}}'$ are the mutual inductances between the excitation coil and detection coil at high frequency f_{h}, before and after the entry of the MO, respectively. $Z_{\mathrm{eh}} = R_{\mathrm{e}}$ and $Z_{\mathrm{dh}} = R_{\mathrm{d}} + R_{\mathrm{dh}}$ are the equivalent impedances of the excitation circuit and detection circuit in resonance. ${Z_{\mathrm{eh}}}'$ and ${Z_{\mathrm{dh}}}'$ are the equivalent impedances of the excitation and detection circuits when the MO is present. $M_{\mathrm{em\text{-}h}}$ and $M_{\mathrm{dm\text{-}h}}$ are the equivalent mutual inductances between the excitation coil and the MO, and between the detection coil and the MO, respectively, at high frequency f_{h}. These parameters can be expressed as

$${Z_{\mathrm{eh}}}' = R_{\mathrm{e}} + \frac{R_{\mathrm{m}}(\omega_{\mathrm{h}} {M_{\mathrm{em-h}}}')^2}{R_{\mathrm{m}}^2 + (\omega_{\mathrm{h}} L_{\mathrm{m}})^2} - j\frac{L_{\mathrm{m}}(\omega_{\mathrm{h}} {M_{\mathrm{em-h}}}')^2}{R_{\mathrm{m}}^2 + (\omega_{\mathrm{h}} L_{\mathrm{m}})^2} + j\omega_{\mathrm{h}} L_{\mathrm{eM}} \tag{17}$$

$${Z_{\mathrm{dh}}}' = R_{\mathrm{d}} + R_{\mathrm{dh}} + \frac{R_{\mathrm{m}}(\omega_{\mathrm{h}} {M_{\mathrm{dm-h}}}')^2}{R_{\mathrm{m}}^2 + (\omega_{\mathrm{h}} L_{\mathrm{m}})^2} - j\frac{L_{\mathrm{m}}(\omega_{\mathrm{h}} {M_{\mathrm{dm-h}}}')^2}{R_{\mathrm{m}}^2 + (\omega_{\mathrm{h}} L_{\mathrm{m}})^2} + j\omega_{\mathrm{h}} L_{\mathrm{dM}} \tag{18}$$

$${M_{\mathrm{ed-h}}}' = M_{\mathrm{ed-h}} - \frac{j\omega_{\mathrm{h}} M_{\mathrm{em-h}} M_{\mathrm{dm-h}}}{R_{\mathrm{m}} + j\omega_{\mathrm{h}} L_{\mathrm{m}}} + \Delta M_{\mathrm{ed}}. \tag{19}$$

From (15) and (16), several conclusions can be drawn. The entry of a MO causes a change in detection voltage, which is mainly due to the changes in mutual inductance between the excitation coil and detection coil. Additionally, the change in the equivalent impedance of the detection coil also contributes to the voltage change. These parameter changes are influenced by the detection frequency, and the magnitude of the voltage change is positively correlated with the input voltage.

B. Analysis of DF-Detection Voltage Variations

When a MO enters the detection system, the mutual inductance M_{ed} between the detection coil and the excitation coil and

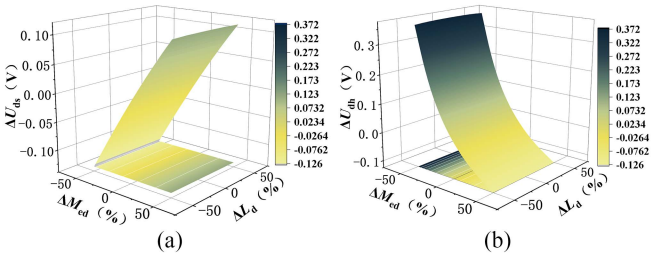

Fig. 10. Effect of MO intrusion on dual-frequency detection voltage. (a) Low-frequency detection voltage. (b) High-frequency detection voltage.

the equivalent impedance Z_d of the detection coil are the main factors causing changes in the sampling voltage. It has been shown in previous studies that the resistance of the detection coil changes very little under a 1 MHz detection magnetic field and can be neglected. Fig. 10 illustrates the effects of variations in M_{ed} and the self-inductance L_d of the detection coil on high and low-frequency sampling voltages.

It can be concluded from Fig. 10 that the variation in the inductance of the detection coil has a relatively minor impact on the detection voltage change. The key factor causing changes in the sampling voltage is the variation in mutual inductance. At a low detection frequency of 8.5 kHz, an increase in mutual inductance causes an increase in the sampling voltage, while a decrease in mutual inductance causes a decrease in the sampling voltage. Conversely, at a high detection frequency of 850 kHz, an increase in mutual inductance results in a decrease in the sampling voltage, and a decrease in mutual inductance results in an increase in the sampling voltage. Thus, it can be concluded that the characteristics of detection voltage variations change at different frequencies. Neglecting the influence of changes in the equivalent impedance of the detection coil on the sampling voltage, the sampling voltage expression U_{dx} can be extended to all frequencies based on (11)

$$U_{dx} = \left| \frac{j\omega M_{ed} U_e R_{dx}}{Z_e Z_d + \omega^2 {M_{ed}}^2} \right| = \frac{U_e R_{dx}}{\frac{R_e(R_d + R_{dx})}{\omega M_{ed}} + \omega M_{ed}}. \quad (20)$$

It can be observed that the detection frequency ω, sampling resistor R_{dx}, internal resistance of the excitation circuit R_e, and internal resistance of the detection circuit R_d determine the trend of changes in the sampling voltage. By differentiating ωM_{ed} with respect to the denominator in the expression for U_{dx} and setting it to zero, the following relationship can be derived:

$$R_e(R_d + R_{dx}) = {\omega_s}^2 {M_{ed}}^2. \quad (21)$$

When $\omega^2 {M_{ed}}^2$ is greater than $R_e(R_d + R_{dx})$, an increase in mutual inductance leads to a decrease in sampling voltage. Conversely, when $\omega^2 {M_{ed}}^2$ is less than $R_e(R_d + R_{dx})$, an increase in mutual inductance leads to an increase in sampling voltage. Therefore, once the system parameters are determined, the trend in sampling voltage changes can be used to judge whether the system's mutual inductance is increasing or decreasing, thereby initially determining whether the metal foreign object is ferromagnetic or nonferromagnetic. The FOs type determination process of DF-MOD is shown in Fig. 11.

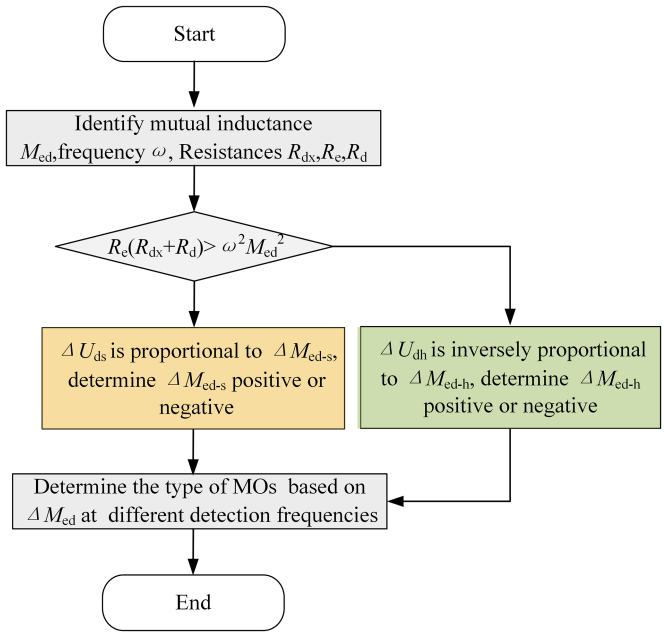

Fig. 11. FOs type determination process of DF-MOD.

TABLE I
VOLTAGE VARIATIONS CHARACTERISTICS OF FOS

FOD	Non-ferromagnetic MOs	Ferromagnetic MOs	Ferrite
$\lvert U_{ds} \rvert$	Decrease	Increase	Increase
$\lvert U_{dh} \rvert$	Increase	Increase	Decrease

For the intruding FOs, when the eddy effect dominates, the ΔM_{ed} decreases; when the magnetization effect dominates, the ΔMed increases. Therefore, according to the DF-detection voltage amplitude $\lvert U_{ds} \rvert$ and $\lvert U_{dh} \rvert$ can be realised to judge the type of FOs, and its dual-frequency voltage variations characteristics are shown in Table I.

C. Analysis of DF-Detection Sensitivity Characteristics

This system detects metal foreign objects by monitoring changes in the induced voltage amplitude. The detection voltage change rate is defined as detection sensitivity. Define S_{ds} as the LF-detection sensitivity, S_{dh} as the HF-detection sensitivity, and S as the DF-detection sensitivity, which can be expressed by

$$S = \mathrm{MAX}(S_{ds}, S_{dh}). \quad (22)$$

When performing MOD, the system selects the higher sensitivity from either LF-detection or HF-detection as the system's detection sensitivity. According to (15) and (16), the specific expressions for high and low-frequency detection sensitivities are obtained

$$S_{ds} = \left| 1 - \frac{{M_{ed-s}}'}{M_{ed-s}} \frac{\left| Z_{es} Z_{ds} + {\omega_s}^2 {M_{ed-s}}^2 \right|}{\left| {Z_{es}}' {Z_{ds}}' + {\omega_s}^2 {M_{ed-s}}'^2 \right|} \right| \times 100\% \quad (23)$$

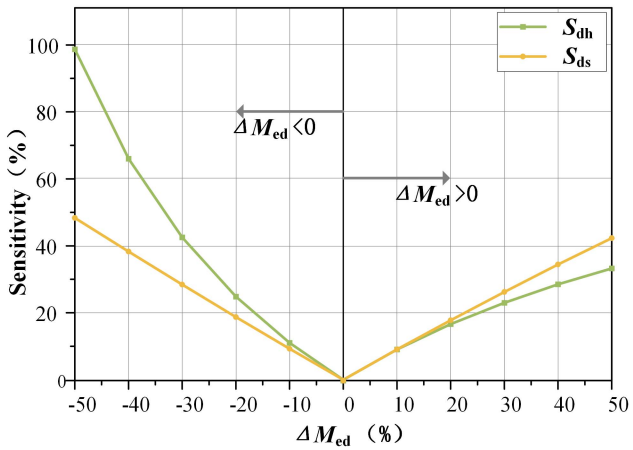

Fig. 12. Relationship between the ΔM_{ed} and sensitivity.

$$S_{\mathrm{dh}} = \left| 1 - \frac{M_{\mathrm{ed-h}}'}{M_{\mathrm{ed-h}}} \frac{\left| Z_{\mathrm{eh}} Z_{\mathrm{dh}} + {\omega_{\mathrm{h}}}^2 {M_{\mathrm{ed-h}}}^2 \right|}{\left| Z_{\mathrm{eh}}' Z_{\mathrm{dh}}' + {\omega_{\mathrm{h}}}^2 {M_{\mathrm{ed-h}}'}^2 \right|} \right| \times 100\%. \tag{24}$$

As previously analyzed, the mutual inductance M_{ed} is the key factor affecting the system's sampling voltage change. Therefore, based on the sensitivity formulas (23) and (24), the DF-detection sensitivity relationship under different mutual inductance changes is shown in Fig. 12.

From Fig. 12, it can be concluded that LF-detection has higher sensitivity for ferromagnetic metals (where magnetization effect is greater than eddy effect), while HF-detection is more effective for nonferromagnetic metals (where eddy effect is greater than magnetization effect). Therefore, this study opts for dual-frequency detection, which not only mitigates the detection failure of certain metals in single-frequency detection but also improves detection sensitivity to some extent.

D. Analysis of DF-Detection Power Characteristics

The SPWM modulation index in the DF-MOD system needs to be optimized by considering both the detection performance and power consumption. When the system is in resonance, the low-frequency current component I_{es} and high-frequency current component I_{eh} in the excitation coil, as well as the low-frequency current component I_{ds} and high-frequency current component I_{dh} in the detection coil, can be determined

$$\begin{cases} I_{\mathrm{es}} = \frac{U_{\mathrm{es}}(R_{\mathrm{d}}+R_{\mathrm{ds}})}{R_{\mathrm{e}}(R_{\mathrm{d}}+R_{\mathrm{ds}})+(\omega_{\mathrm{s}}M_{\mathrm{ed-s}})^2} \\ I_{\mathrm{eh}} = \frac{U_{\mathrm{eh}}(R_{\mathrm{d}}+R_{\mathrm{dh}})}{R_{\mathrm{e}}(R_{\mathrm{d}}+R_{\mathrm{dh}})+(\omega_{\mathrm{h}}M_{\mathrm{ed-h}})^2} \\ I_{\mathrm{ds}} = \frac{j\omega_{\mathrm{s}}M_{\mathrm{ed-s}}U_{\mathrm{es}}}{R_{\mathrm{e}}(R_{\mathrm{d}}+R_{\mathrm{ds}})+(\omega_{\mathrm{s}}M_{\mathrm{ed-s}})^2} \\ I_{\mathrm{dh}} = \frac{j\omega_{\mathrm{h}}M_{\mathrm{ed-h}}U_{\mathrm{eh}}}{R_{\mathrm{e}}(R_{\mathrm{d}}+R_{\mathrm{dh}})+(\omega_{\mathrm{h}}M_{\mathrm{ed-h}})^2}. \end{cases} \tag{25}$$

Furthermore, the power consumption P_{loss} of the DF-MOD system can be calculated

$$P_{\mathrm{loss}} = \left({I_{\mathrm{es}}}^2 + {I_{\mathrm{eh}}}^2\right) R_{\mathrm{e}} + {I_{\mathrm{ds}}}^2 (R_{\mathrm{e}} + R_{\mathrm{ds}}) + {I_{\mathrm{dh}}}^2 (R_{\mathrm{e}} + R_{\mathrm{dh}}). \tag{26}$$

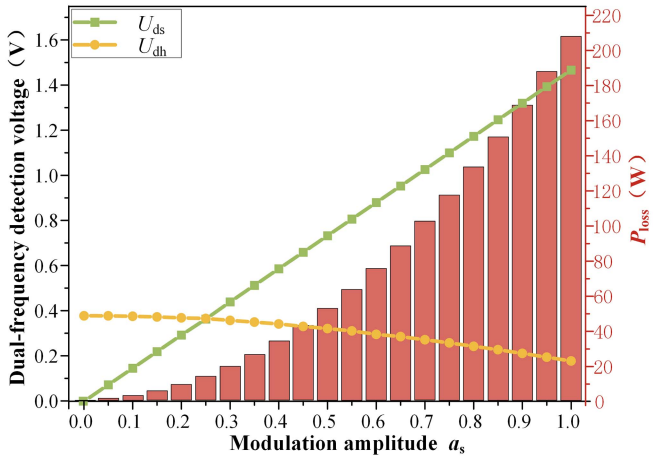

Fig. 13. Effect of modulation amplitude a_{s} on DF-MOD systems.

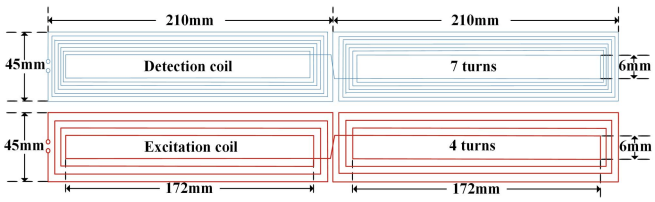

Fig. 14. Specification of detection and excitation coil.

In this system, the dc operating voltage V_{in} is set to 10 V, and both the low-frequency sampling resistor and the high-frequency sampling resistor are set to 1 Ω. The relationship between the dual-frequency sampling voltages U_{ds} and U_{dh} in the detection coil, as well as the system power P_{loss} and the modulation index, is shown in Fig. 13.

As shown in Fig. 13, once the system parameters are determined, the system power increases sharply with the modulation index. When the modulation index is around 0.2, the LF-sampling voltage and the HF-sampling voltage are approximately equal, making it easier to observe the DF-detection voltage changes. At this point, the system power consumption is relatively low. Therefore, in this article, the SPWM modulation index for the DF-MOD system is designed to be 0.2.

IV. System Parameter Design

A. Design of Main Circuit Parameter

The detection coil employs two spiral rectangular subcoils in a reverse series connection structure. Referring to the coil size design method in [13], and based on the dimensions of the emission coil (580×420 mm) and the typical sizes of MO, the coil specifications are determined, as shown in Fig. 14.

The spacing of detection coil wires is 2 mm, and the spacing of excitation coil wires is 5 mm. Each turn of the coil has a width of 2 mm, with the subcoils connected via the lower layer of the printed circuit board (PCB). Under these specifications, the measured inductance of the excitation coil is 4.96 μH, and the inductance of the detection coil is 14.72 μH. The parasitic

TABLE II
PARAMETERS OF DF-RESONANT AND SAMPLING CIRCUITS

Parameter	Value	Parameter	Value
C_{es}	700.0 nF	R_{ds}	1.0 Ω
L_{ep}	486.1 μH	L_s	14.7 μH
C_{ep}	6.8 μF	C_s	23.8 μF
L_h	14.7 μH	C_{dh}	2.4 nF
C_h	2.4 nF	R_{dh}	1.0 Ω
C_{ds}	11.9 μF	V_{in}	10.0 V

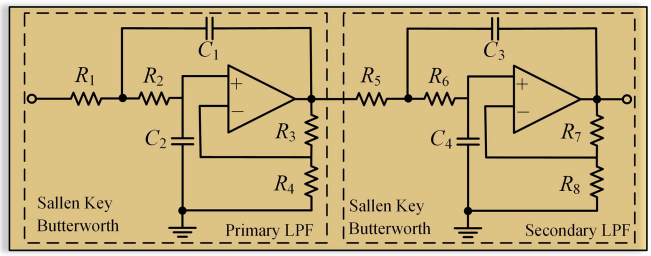

Fig. 15. Circuit diagram of the LPF.

resistance generated by the inductor in the sampling circuit will affect the design of the parallel resonance parameters of the wave blocking circuit. As the system is also set up with an active filter circuit to filter out the interference signals of other frequencies, the dual-frequency crosstalk rate is less than 5% as an index, and it is sufficient to satisfy the conditions. Based on (5)–(7), the parameters of the DF-resonant circuit and DF-sampling circuit are designed, as shown in Table II.

Simulation analysis by Simulink under these parameters shows that the high-frequency voltage content in the low-frequency sampling voltage is 1.51% of the low-frequency voltage. The low-frequency voltage content in the high-frequency sampling voltage is less than 1% of the high-frequency voltage. This achieves the wave-trapping function of the DF-sampling circuit. However, fast Fourier transform (FFT) analysis results indicate that the harmonic content near twice the carrier frequency (1.7 MHz, or $2f_c \pm f_s$) significantly affects the sampling voltage. Therefore, an active filter circuit is used next to eliminate the harmonic.

B. Design of Filter Circuit Parameter

1) Design of LPF Circuit Parameter: This system designs a second-order LPF circuit in series to form a fourth-order LPF circuit. This setup reduces interference signals at other frequencies from affecting the low-frequency detection signal. The LPF circuit is shown in Fig. 15.

Analyzing primary LPF, resistors R_3, R_4, and the operational amplifier form a noninverting amplifier, called a voltage-controlled voltage source. The voltage-controlled gain K_s is expressed as

$$K_s = 1 + \frac{R_3}{R_4}. \tag{27}$$

The natural frequency ω_s and quality factor Q_s are core parameters of the second-order LPF circuit. These parameters

TABLE III
PARAMETERS OF LPF

Parameter	Value	Parameter	Value
R_1	6.8 kΩ	R_5	3.6 kΩ
R_2	110 kΩ	R_6	27 kΩ
R_3	5 kΩ	R_7	7.5 kΩ
R_4	5 kΩ	R_8	2 kΩ
C_1	1.6 nF	C_3	1.6 nF
C_2	200 nF	C_4	1.6 nF

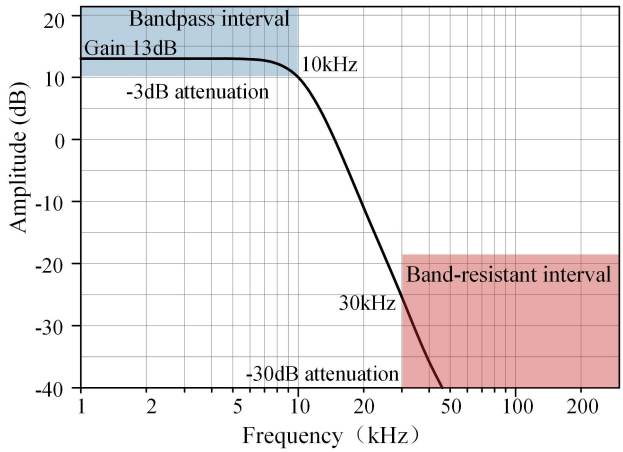

Fig. 16. Amplitude-frequency characteristic curve of the LPF.

directly affect the filter's performance and are related to the circuit components as follows:

$$\omega_s = \frac{1}{\sqrt{R_1 R_2 C_1 C_2}} \tag{28}$$

$$\frac{\omega_s}{Q_S} = \frac{1}{C_1}\left(\frac{R_1 + R_2}{R_1 R_2}\right) + \frac{1 - K_s}{R_2 C_2}. \tag{29}$$

It is important to note that due to the positive feedback in the voltage-controlled voltage source circuit, the voltage-controlled gain cannot be designed too large, or it will lead to circuit self-oscillation. Table III shows the parameters of the LPF circuit designed for this system.

Based on the abovementioned parameters, the amplitude-frequency characteristics of the designed LPF circuit can be obtained through Multisim simulation, as shown in Fig. 16.

From Fig. 16, it can be seen that the LPF circuit attenuates signals at 85 kHz and above by more than −40 dB. This effectively filters out interference from the power magnetic field and high-frequency detection signals.

2) Design of BPF Circuit Parameter: To eliminate the harmonic components near twice the carrier frequency in the inverter output voltage, a BPF circuit is designed, as shown in Fig. 17.

By cascading second-order band-pass filter circuits, a fourth-order BPF circuit that satisfies the requirements can be obtained. Taking a single-stage BPF as an example, the filtering parameters of the second-order multiple feedback band-pass filter circuit, such as gain K_h, natural frequency ω_h, and quality factor Q_h,

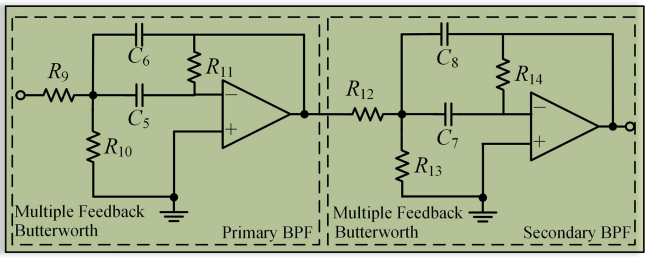

Fig. 17. Circuit diagram of the BPF.

TABLE IV
PARAMETERS OF BPF

Parameter	Value	Parameter	Value
R_9	43 kΩ	R_{12}	43 kΩ
R_{10}	560 Ω	R_{13}	560 kΩ
R_{11}	180 kΩ	R_{14}	180 kΩ
C_5	18pF	C_7	18 pF
C_6	18 pF	C_8	18 pF

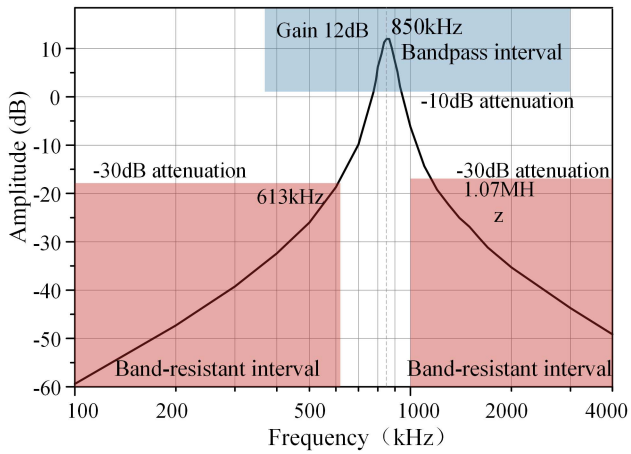

Fig. 18. Amplitude-frequency characteristic curve of the BPF.

are related to the circuit components as follows:

$$K_{\mathrm{h}} = -\frac{C_5 R_{11}}{R_9(C_5 + C_6)} \tag{30}$$

$$\omega_{\mathrm{h}} = \sqrt{\frac{R_9 + R_{10}}{R_9 R_{10} R_{11} C_5 C_6}} \tag{31}$$

$$\frac{\omega_{\mathrm{h}}}{Q_{\mathrm{h}}} = \frac{C_5 + C_6}{R_{11} C_5 C_6}. \tag{32}$$

The BPF circuit is designed based on the center frequency of 850 kHz, and its parameters are shown in Table IV.

Fig. 18 shows the amplitude-frequency characteristics of the BPF circuit designed in this study. As demonstrated, the filter provides sufficient attenuation of interference signals, thereby satisfying the design requirements.

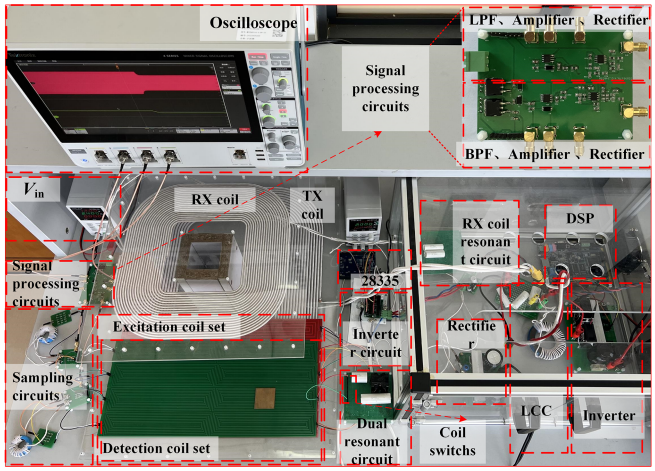

Fig. 19. Platform of the proposed MOD system.

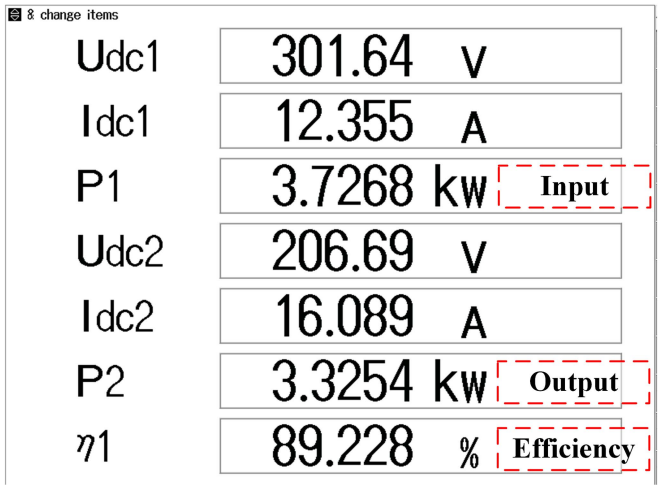

Fig. 20. Output power and efficiency of WEVC system.

V. EXPERIMENTAL VERIFICATION

A. Establishment of Experimental Platform

To validate the feasibility of the SPWM-controlled DF-MOD technology proposed in this article for an WEVC, an experimental setup based on the SAE J2954 standard was established. This setup was used to verify the performance of MOD. Fig. 19 shows the experimental setup of the system.

In Fig. 19, the detection coils do not fully cover the detection area to display the stacked coil structure. Actually, both the set of excitation coils group and the set of detection coils fully cover the transmission coil. Fig. 20 shows the transmission power and efficiency of the WEVC system when operating at 85 kHz.

B. Independent Operation Verification of the DF-MOD System

To verify the independent operational characteristics of the DF-MOD system, the SPWM modulation wave was set to an 8.5 kHz sine wave, with a carrier wave of 850 kHz triangle wave, and a modulation index of 0.2. When the system is in

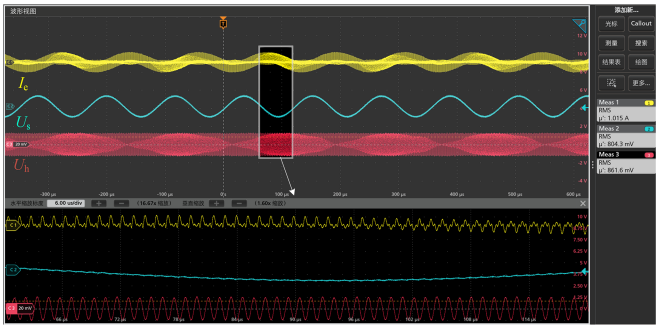

Fig. 21. Waveforms of excitation coil current and filter circuit output voltage.

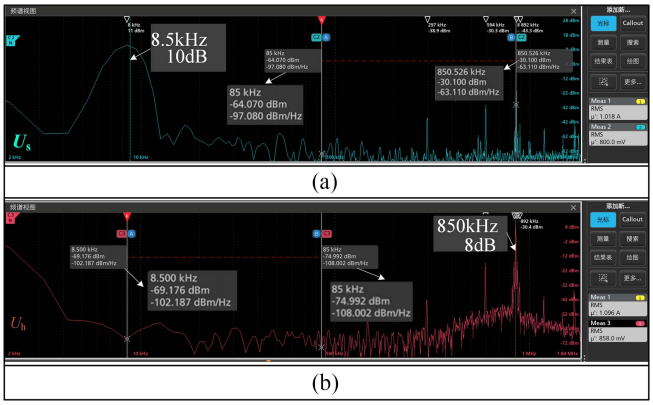

Fig. 22. Spectral distribution output voltage of LPF and BPF. (a) Spectral distribution output voltage of LPF. (b) Spectral distribution output voltage of BPF.

operation, the waveform of the current I_e through the excitation coil and the waveform of the dual-frequency detection voltage signals U_s and U_h of passing through the filter circuit are shown in Fig. 21.

Fig. 21 demonstrates that when the modulation index is 0.2, the current I_e flowing through the excitation coil is a high-frequency 850 kHz carrier wave enveloped by an 8.5 kHz sine wave. This is due to the design of the DF-resonant circuit in the excitation coil circuit. The low-frequency detection voltage U_s and high-frequency detection voltage U_h output by the DF-sampling circuit and the active filter circuit successfully achieve the generation, reception, and separation of dual-frequency detection signals. To further verify the anti-interference capability of the DF-MOD system, spectrum distribution was performed on the dual-frequency signal output from the active filter circuit, as shown in Fig. 22.

As shown in Fig. 22, when the WEVC system and the DF-MOD system are operating simultaneously. The gain of LPF is 10 dB for the 8.5 kHz signal, and the attenuation is −30.1 dB for the 850 kHz signal and 64.1 db for the 85 kHz signal, while the gain of BPF is 8 db for the 850 kHz signal, and the attenuation is −69.2 dB for the 8.5 kHz signal and −74.9 dB for the 85 kHz signal. The signal-to-noise ratio of the BPF and LPF are more than 40 dB. This verifies the independent operational characteristics of the DF-MOD system.

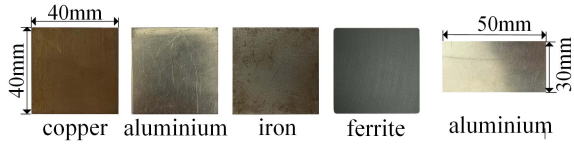

Fig. 23. FOs used in this experiment.

Fig. 24. Detection voltage signal variations of different FOs intrusion. (a) 40 × 40 mm copper intrude. (b) 40 × 40 mm aluminium intrude. (c) 40 × 40 mm iron intrude.

Furthermore, the dual-frequency signal U_s and U_h are amplified and rectified to output dc detection voltage signals U_{DS} and U_{DH}. After running for a certain period, it was observed that the range of dc detection voltage variations remained within 20 mV. Therefore, the threshold voltage of the DF-MOD system is set to 20 mV, and when the variation of the dc detection voltage is larger than the threshold voltage, it can be judged that the foreign object is interfering.

C. Functional Verification of the DF-MOD System

To verify the voltage variation characteristics and sensitivity of the DF-MOD system, a FO was placed in the same position within the detection coil, as shown in Fig. 23, and the changes of detection voltage signals were observed.

Fig. 24 shows the changes in detection signals after the entry of FOs. Before FOs intervention, the LF-detection dc voltage is 1.910 V and the HF-detection dc voltage is 2.125 V.

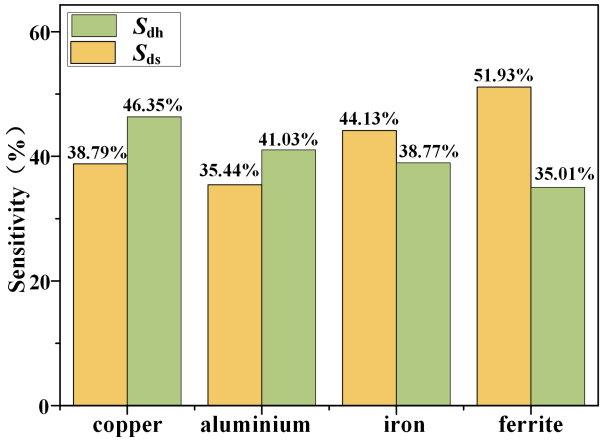

Fig. 25. Sensitivity of DF-MOD.

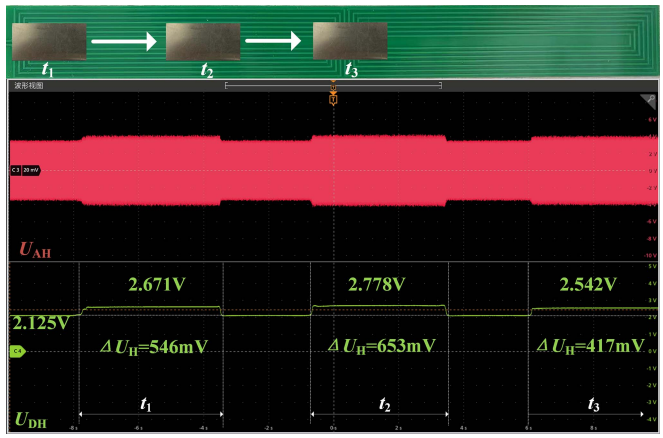

Fig. 26. Detection voltage when MO in different positions of the center of detection coil.

Based on the voltage variation trends for different FOs, the following conclusions were drawn.

1) In the proposed DF-MOD system, when the nonferromagnetic MO (copper plate and aluminum plate) enters, the low-frequency detection voltage decreases, while the high-frequency detection voltage increases.
2) When the ferrite plate enters, the low-frequency detection voltage increases, while the high-frequency detection voltage decreases.
3) When the ferromagnetic MO (iron plate) enters, both the low-frequency and high-frequency detection voltages increase. This is because the iron plate exhibits a magnetization effect at low frequencies and an eddy current effect at high frequencies.

Therefore, the type of FOs can be preliminarily identified based on the trend of changes in dual-frequency detection voltage.

When the above FOs entered into the detection coil, the low-frequency detection voltage changed by −741 mV, −677 mV, 843 mV, and 992 mV, respectively, while the high-frequency detection voltage changed by 985 mV, 872 mV, 824 mV, and −744 mV, respectively. This confirms the effective detection of these FOs.

Based on the detection voltage changes when the four types of FOs, the sensitivity of the DF-MOD system was calculated using the sensitivity formula, as shown in Fig. 25.

It can be seen that the sensitivity of DF-MOD is significantly improved compared to single-frequency detection and eliminates the phenomenon of detection failure for ferromagnetic metals.

To further verify the advantage of the bipolar detection coil without a central detection blind spot, a strip of aluminum (30×50 mm) was placed at the center of the detection coil and moved from the lowest end of the coil to the center, as shown in Fig. 26. Then move the plate to the symmetric positions of the two subcoils. The corresponding times were t_1, t_2, and t_3.

As shown in Fig. 26, the voltage variations corresponding to t_1, t_2, and t_3 were 546 mV, 653 mV, and 417 mV, respectively. The minimum detection sensitivity was 19.62%. This demonstrates that the bipolar coil design eliminates the detection blind spot at the symmetric center of the balanced coil.

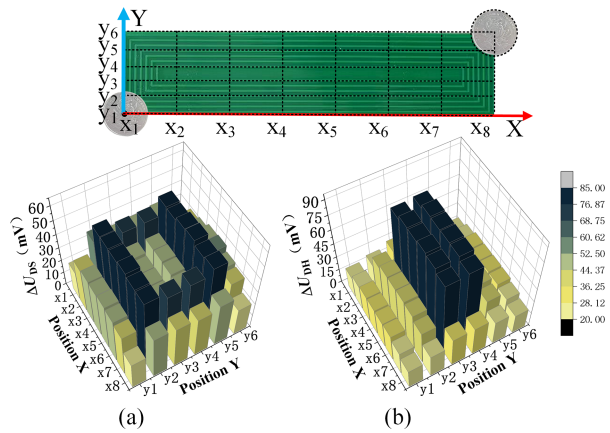

Fig. 27. Full-area detection voltage variations on 1 yuan coin. (a) Low-frequency detection voltage variations ΔU_{DS}. (b) High-frequency detection voltage variations ΔU_{DH}.

To further verify the full-area detection capability of DF-MOD for tiny MOs, a 1 yuan coin was placed at different positions in the detection coil, corresponding to the low-frequency dc detection voltage variations ΔU_{DS} and high-frequency dc detection voltages variations ΔU_{DH}, as shown in Fig. 27(a) and (b).

As shown in Fig. 27, the ΔU_{DS} and ΔU_{DH} are greater than the threshold voltage, realizing high sensitivity detection in the whole area. And according to the trend of dual-frequency detection voltage variations of the coin in different positions of the detection coil, it can be seen that dual-frequency detection can also complementarily improve the detection sensitivity of the entire coil.

VI. Conclusion

This article proposes a DF-MOD technology for EV wireless charging systems controlled by SPWM. By utilizing SPWM modulation technology, designing DF-resonant circuit and sampling circuit, DF-MOD is achieved. The detection voltage variation characteristics and sensitivity characteristics of the

DF-MOD system were analyzed. By optimizing coil dimensions and designing filter circuits, detection sensitivity, and anti-interference capability were improved.

Experimental results demonstrate that this system operates independently from the wireless charging system, eliminating magnetic field detection blind spots and frequency detection failures. The voltage variation characteristics and sensitivity characteristics of different foreign objects under high and low-frequency detection were verified. Compared to single-frequency detection, this system improved the detection sensitivity for 40×40 mm copper plates, aluminum plates, iron plates, and ferrite plates by 7.56%, 5.59%, 5.36%, and 16.82%, respectively. Additionally, the changes in high and low-frequency detection voltages can preliminarily identify the type of MO, providing practical significance for the promotion of EV wireless charging applications.

Since the system can only realize the accurate detection of one-dollar coins and larger size metal objects. In the subsequent research, it is necessary to improve the detection accuracy of the system and its ability to detect tiny foreign objects by further optimizing the coil size and structure, signal processing circuitry, and working logic, so as to promote the development of MOD in WEVC application scenarios.

REFERENCES

[1] S. Gnanavendan et al., "Challenges, solutions and future trends in EV-technology: A review," *IEEE Access*, vol. 12, pp. 17242–17260, 2024.

[2] A. Mahesh, B. Chokkalingam, and L. Mihet-Popa, "Inductive wireless power transfer charging for electric vehicles–a review," *IEEE Access*, vol. 9, pp. 137667–137713, 2021.

[3] M. Wu et al., "A compact coupler with integrated multiple decoupled coils for wireless power transfer system and its anti-misalignment control," *IEEE Trans. Power Electron.*, vol. 37, no. 10, pp. 12814–12827, Oct. 2022.

[4] T. Meng, L. Tan, R. Zhong, H. Xie, and X. Huang, "Research on metal foreign object detection of electric vehicle wireless charging system based on detection coil," *World Electric Veh. J.*, vol. 12, no. 10, pp. 12–203, Oct. 2021.

[5] Z. Zhang, H. Pang, A. Georgiadis, and C. Cecati, "Wireless power transfer—An overview," *IEEE Trans. Ind. Electron.*, vol. 66, no. 2, pp. 1044–1058, Feb. 2019.

[6] W. Zhong, F. Xiang, and C. Hu, "Metal object detection with detection coils perpendicular to power coils for wireless power transfer systems," *IEEE Trans. Power Electron.*, vol. 38, no. 9, pp. 10530–10534, Sep. 2023.

[7] Z. Yang, C. Xia, S. Zhao, H. Lu, C. Hu, and X. Huang, "Receiver position detection system of wireless electric vehicle charger based on novel active beacon structure," *IEEE Trans. Ind. Electron.*, vol. 71, no. 10, pp. 13450–13460, Oct. 2024.

[8] Y. Sun, K. Song, T. Zhou, G. Wei, Z. Cheng, and C. Zhu, "A shared method of metal object detection and living object detection based on the quality factor of detection coils for electric vehicle wireless charging," *IEEE Trans. Instrum. Meas.*, vol. 72, 2023, Art. no. 9002517.

[9] J. Lu, G. Zhu, and C. C. Mi, "Foreign object detection in wireless power transfer systems," *IEEE Trans. Ind. Appl.*, vol. 58, no. 1, pp. 1340–1354, Jan./Feb. 2022.

[10] B. Long, Q. Zhu, S. Zang, L. Zhao, and A. P. Hu, "Metal object detection by monitoring fifth-order harmonic current of IPT system with dual frequency tuning," *IEEE Trans. Power Electron.*, vol. 37, no. 3, pp. 2513–2518, Mar. 2022.

[11] Y. Zhang, Z. Yan, J. Zhu, S. Li, and C. Mi, "A review of foreign object detection (FOD) for inductive power transfer systems," *eTransportation*, vol. 1, p. 100002, 2020.

[12] H. Chen, C. Liu, Y. Zhang, S. Liu, J. Wu, and X. He, "Metal object and vehicle position detections integrated with near-field communication for wireless EV charging," *IEEE Trans. Veh. Technol.*, vol. 71, no. 7, pp. 7134–7146, Jul. 2022.

[13] S. Zhao, C. Xia, Z. Yang, H. Li, and Y. Cao, "Evaluation modeling and improvement method for sensitivity of metal object detection in EV wireless charging system," *IEEE Trans. Power Electron.*, vol. 39, no. 3, pp. 3809–3825, Mar. 2024.

[14] V. X. Thai, J. H. Park, S. Y. Jeong, C. T. Rim, and Y.-S. Kim, "Equivalent-circuit-based design of symmetric sensing coil for self-inductance-based metal object detection," *IEEE Access*, vol. 8, pp. 94190–94203, 2020.

[15] S. Y. Jeong, V. X. Thai, J. H. Park, and C. T. Rim, "Self-inductance-based metal object detection with mistuned resonant circuits and nullifying induced voltage for wireless EV chargers," *IEEE Trans. Power Electron.*, vol. 34, no. 1, pp. 748–758, Jan. 2019.

[16] L. Li, J. Wang, C. Cai, Z. Lin, M. Hu, and F. Zhang, "Phase-detection-based metal objects and pick-up coils detection scheme without malfunction in wireless power transfer system," *IET Electric Power Appl.*, vol. 14, pp. 2222–2230, Sep. 2020.

[17] C. Xia et al., " Planar double-winding foreign object detection for the EV wireless charging system based on time-division multiplexing," *IEEE Trans. Power Electron.*, vol. 39, no. 10,pp. 13988–14004, Oct. 2024.

[18] Y. Sun, G. Wei, K. Qian, P. He, C. Zhu, and K. Song, "A foreign object detection method based on variation of quality factor of detection coil at multi-frequency," in *Proc. IEEE 12th Energy Convers. Congr. Expo. - Asia*, Singapore, 2021, pp. 1578–1582.

[19] L. Xiang, Z. Zhu, J. Tian, and Y. Tian, "Foreign object detection in a wireless power transfer system using symmetrical coil sets," *IEEE Access*, vol. 7, pp. 44622–44631, 2019.

[20] S. Niu, S. Niu, C. Zhang, and L. Jian, "Blind-zone-free metal object detection for wireless EV chargers employing DD coils by passive electromagnetic sensing," *IEEE Trans. Ind. Electron.*, vol. 70, no. 1, pp. 965–974, Jan. 2023.

[21] C. Qi, T. Lin, Z. Wang, D. Li, and T. Sun, "Research on metal object detection of MCR-WPT system that allows transmisson coils to be misaligned," in *Proc. 45th Annu. Conf. IEEE Ind. Electron. Soc.*, Lisbon, Portugal, 2019, pp. 4642–4647.

[22] S. Zhao, C. Xia, Z. Yang, H. Lu, H. Zhang, and C. Lu, "Bipolar checkerboard metal object detection without blind zone caused by excitation magnetic field for stationary EV wireless charging system," *IEEE Trans. Power Electron.*, vol. 38, no. 5, pp. 6696–6709, May 2023.

[23] C. Xia, N. Wei, H. Zhang, S. Zhao, Z. Li, and Z. Liao, "Multifrequency and multiload MCR-WPT system using hybrid modulation waves SPWM control method," *IEEE Trans. Power Electron.*, vol. 36, no. 11, pp. 12400–12412, Nov. 2021.

[24] C. Xia et al., "Simultaneous wireless power and multibit signals transfer system with hybrid modulation waves PWM control," *IEEE Trans. Power Electron.*, vol. 37, no. 10, pp. 12913–12928, Oct. 2022.

[25] Y. Tian et al., "A review on foreign object detection for magnetic coupling-based electric vehicle wireless charging," *Green Energy Intell. Transp.*, vol. 1, no. 2, pp. 2773–1537, Sep. 2022.

Chenyang Xia (Member, IEEE) was born in Jiangsu Province, China, in 1982. He received the B.S., M.S., and Ph.D. degrees in control theory and control engineering from Chongqing University, Chongqing, China, in 2006, 2008, and 2010, respectively.

From 2018 to 2019, he was an Academic Visitor with the University of Auckland, Auckland, New Zealand. He is currently a Professor with the School of Electrical Engineering, China University of Mining and Technology, Xuzhou, China. His research interests include wireless power transfer and intelligent control.

Yuheng Cao received the B.S. degree in electrical engineering from Shanghai DianJi University, Shanghai, China, in 2022. He is currently working toward the M.S. degree in electrical engineering with the School of Electrical Engineering, China University of Mining and Technology, Xuzhou, China.

His research interest includes wireless power transfer.

Ziyue Yang received the B.S. degree in electrical engineering in 2020 from China University of Mining and Technology, Xuzhou, China, where he is currently working toward the Ph.D. degree in electrical engineering with the School of Electrical Engineering.

His research interest includes wireless power transfer.

Shuze Zhao received the B.S. degree in electrical engineering in 2018 from China University of Mining and Technology, Xuzhou, China, where he is currently working toward the Ph.D. degree in electrical engineering with the School of Electrical Engineering.

His research interest includes wireless power transfer.

Xirui Wang received the B.S. degree in electrical engineering in 2023 from China University of Mining and Technology, Xuzhou, China, where she is currently working toward the M.S. degree in electrical engineering with the School of Electrical Engineering.

Her research interest includes wireless power transfer.

Chenhao Lu received the B.S. degree in electrical engineering in 2022 from China University of Mining and Technology, Xuzhou, China, where he is currently working toward the M.S. degree in electrical engineering with the School of Electrical Engineering.

His research interest includes wireless power transfer.

Leilei Liu received the B.S. degree in electrical engineering from Anhui Polytechnic University, Xuzhou, China, in 2022. He is currently working toward the M.S. degree in electrical engineering with the School of Electrical Engineering, China University of Mining and Technology, Xuzhou, China.

His research interest includes wireless power transfer.